Tunable hierarchical TiO2 nanostructures by controlled annealing of electrospun fibers : formation mechanism, morphology, crystallographic phase and photoelectrochemical performance analysis

Kumar, Palaniswamy Suresh; Nizar, S. A. Syed; Sundaramurthy, Jayaraman; Ragupathy, P.; Thavasi, V.; Mhaisalkar, Subodh Gautam; Ramakrishna, Seeram

2011

Kumar, P. S., Nizar, S. A. S., Sundaramurthy, J., Ragupathy, P., Thavasi, V., Mhaisalkar, S. G., et al. (2011). Tunable hierarchical TiO2 nanostructures by controlled annealing of electrospun fibers : formation mechanism, morphology, crystallographic phase and photoelectrochemical performance analysis. Journal of materials chemistry, 21, 9784-9790.

https://hdl.handle.net/10356/94961

https://doi.org/10.1039/C1JM10859J

Journal of
Materials Chemistry

Dynamic Article Links

Cite this: DOI: 10.1039/c0xx00000x

www.rsc.org/xxxxxx

ARTICLE TYPE

Tunable hierarchical TiO_2 nanostructures by controlled annealing of electrospun fibers: formation mechanism, morphology, crystallographic phase and photoelectrochemical performance analysis

P. Suresh Kumar,[a] S. A. Syed Nizar,[c] J. Sundaramurthy,[a] P. Ragupathy,[a] V. Thavasi,*[c] S. G. Mhaisalkar[a] and S. Ramakrishna*[b]

Received (in XXX, XXX) Xth XXXXXXXXX 20XX, Accepted Xth XXXXXXXXX 20XX
DOI: 10.1039/b000000x

Highly crystalline hierarchical TiO_2 nanostructures of morphology ranging from one-dimensional regular fibers, hollow tubes, porous rods and spindles were achieved from electrospun TiO_2/composite fibers by annealing at temperatures ranging from 400 °C, 500 °C, 600 °C, 700 °C, and 800 °C, with a ramp rate of 5 °C min^{-1}, and at a pressure of 1 mbar. Crystallographic structure, crystallite size, surface morphology and surface area of annealed TiO_2 nanostructures were analysed by X-ray powder diffraction (XRD), field emission scanning electron microscopy (FESEM), high-resolution transmission electron microscopy (HRTEM) and Brunauer–Emmett–Teller (BET) method. The analysis of post-annealing process on electrospun TiO_2 nanofibers showed an orderly change in the crystallographic phase transformation with corresponding change in their surface morphologies. XRD and HRTEM analysis confirmed the phase transformation of highly crystalline anatase phase to rutile with crystallite size varied from 11 nm to 36 nm upon tuning the annealing temperature. Interestingly, TiO_2 nanostructures annealed at 700 °C showed the formation of biphasic TiO_2 hollow tubes with stoichiometry phase compositions of 45.74% anatase and 54.25% rutile. A possible formation mechanism was proposed based on series of temperature-dependent experiments. To evaluate the potential use of these TiO_2 nanostructures, dye sensitized solar cell (DSSC) was fabricated using the post-annealed TiO_2 nanostructures as photoanode. A higher conversion efficiency (η) of 4.56% with a short circuit current (J_{sc}) of 8.61 mA cm^{-2} was observed for highly ordered porous anatase TiO_2 nanorods obtained upon annealing at 500 °C under simulated AM1.5 G (100 mW cm^{-2}), confirming that surface area of TiO_2 resulted out of porous structure played dominant role.

1. Introduction

Recently, nanomaterials with different morphologies and polymorphs have attracted great interest as their optical and electrical properties strongly depend on shape, size, and phase composition. The ability to manipulate and control these hierarchical structures such as nanowires, nanotubes, nanobelts, nanorods, nanospheres and nanoflowers has developed many new classes of material properties useful for challenging application domains such as nano-energy and electronic devices.[1] Among various functional oxide semiconductors, TiO_2 based hierarchical or/and ordered architectures were found to be superior for photoelectrochemical performance due to their efficiency in charge collection and slower charge recombination. Anatase, rutile, and brookite are the three polymorphs of TiO_2 which differ only in the arrangement of their $[TiO_6]^{2-}$ octahedral vertices. Anatase (tetragonal) consists of octahedral sharing vertices with an indirect band gap of 3.2 eV; rutile (tetragonal) is connected by edges and has the direct band gap of 3.0 eV, whereas in brookite (orthorhombic) both edges and vertices are connected and has a direct transition with a band gap energy of 3.4 eV. They are promising for multifunctional applications such as environmental remediation, dye-sensitized solar cells (DSSCs), biosensors, storage devices, antimicrobial coatings and self-cleaning coatings.[2–8] Anatase phase TiO_2 is thermodynamically more stable phase with higher electron mobility and low surface Gibbs free energy than rutile, which makes more suitable for solar cell performance. The effect of shape, size and crystallographic phase of TiO_2 nanostructures have been studied extensively and recent

[a]*School of Materials Science and Engineering, Nanyang Technological University, 50 Nanyang Avenue, Singapore 639798*
[b]*Mechanical Engineering, National University of Singapore, Singapore 117576. E-mail: seeram@nus.edu.sg; velnanotech@gmail.com; Fax: +65 6872 5563; Tel: +65 6516 6593*
[c]*NUS Nanoscience and Nanotechnology Initiative, National University of Singapore, Singapore 117576*

literatures on rutile and mixed phase (anatase–rutile) have shown better electrochemical characteristics than those of anatase phase.[9,10]

Kim *et al.*[11] have successfully synthesized TiO_2 hollow nanoribbons from a peptide assembly using atomic layer deposition and demonstrated as a promising electrode material for high-performance Li batteries. Shao *et al.*[12] have developed TiO_2 nanorod arrays, nanobelt arrays, and fan-shaped rectangular parallelepiped rods using the alkali hydrothermal method by changing the concentration of alkali solution, and obtained higher conversion efficiency (6.0%) for the highly ordered TiO_2 nanorods array. Sauvage *et al.*[13] have adopted PLD for the synthesis of mimic trees TiO_2 morphology, which yielded the conversion efficiency of 3.1% for only 2 μm thick TiO_2 film and 5% for 7 μm thick film. These hierarchical photoanode nanostructures exhibit a large surface area for the adsorption of the dye which enhances light harvesting efficiency by scattering more light in the red part of the solar spectrum.[14] Shorter electron-transport time and longer electron diffusion length are the critical factors for the improvement of power conversion efficiency of DSSCs. Moreover, the efficiency of solar cell was also improved by surface modification due to the formed barrier layer, which can reduce the dark current contributed by the interfacial charger combination. So far, various physical and chemical methods include thermal evaporation,[15] plasma enhanced chemical vapour deposition,[16] atomic layer deposition,[17] hydrothermal,[18] and solution phase[19] have been adopted to prepare a variety of morphological TiO_2 nanostructures. However, the synthesis of the TiO_2 hierarchical architectures either involves stringent reaction conditions or complicated process conditions like ultra high vacuum (10^{-12} torr) and low temperature, often induces low crystalline growth and high surface defects in the TiO_2 structures, which can cause high recombination rate of electron (e^-) and hole (h^+), and shorten carrier lifetime that dampen the device efficiency.

In addition to these growth methodologies, morphology effects has also been greatly influenced by ion irradiation, templates, applied potential, concentration, pH, surfactants, capping agents and change the properties.[20–23] The presence of templates, surfactants, or other additives in the end products not only increases the production cost but also makes it more difficult to scale-up. Electrospinning has emerged as a versatile means of generating one dimensional (1D) fibrous structure with typical diameter varying from nm to μm, with several advantages over other methods; large-area applicability, environmental friendliness and room temperature process. In the present study, we adopted systematic and controlled post-annealing based electrospinning process to synthesize hierarchical TiO_2 photoanode architectures. We found that the crystallinity, crystallographic phase of TiO_2 and their electrochemical performance in liquid state DSSC were influenced by the surface morphologies of TiO_2.

2. Experimental details

(a) Materials and synthesis process

Titanium(IV) isopropoxide (99%) and *N*,*N*-dimethyl formamide (DMF, 99.8%), polyvinyl acetate (PVAc, MW: 5×10^5) and 100% pure acetic acid were purchased from Aldrich and used as received without any further purification. The simple electrospinning process involves the application of a strong electrostatic field to a capillary connected with a precursor solution. The fiber diameter could be tailored by controlling the injection rate and electric field. The fiber diameter also depends on the intrinsic properties of the polymeric solution such as viscosity and surface charge. In our study, 12 wt% of PVAc was dissolved in 20 ml DMF and stirred for an hour to make a homogeneous solution. 0.75 M of titanium(IV) isopropoxide solution was added dropwise followed by the addition of glacial acetic acid. The solution pH was maintained at 6 and the precursor solution mixture was stirred for overnight. As-prepared solution was introduced in 5 ml syringe with a needle diameter of 11.9 mm in a controlled electrospinning setup (ELECTROSPUNRA, Microtools Pvt. limited, Singapore). The distance between needle and static collector (aluminium foil) was maintained at 10 cm with an applied ac voltage of 15 kV and at a flow rate of 1 ml h^{-1}. Under the influence of electrostatic field, a pendant droplet of the precursor solution at the capillary tip was deformed into a conical shape (Taylor cone). At 15 kV, the electrostatic forces overcame the surface tension of the polymer blend, and a fine charged/jet was ejected. The jet moved towards a grounded plate which acts as counter electrode, and dried to form the TiO_2/PVAc composite fibers. The electrospun TiO_2 composite fibers were annealed at temperatures from 400 to 800 °C with 100 °C as interval with a ramp rate of 5 °C min^{-1} and at a pressure of 1 mbar for 1 h using carbolite furnace.

(b) Device fabrication

To fabricate DSSC, the post-annealed electrospun hierarchical TiO_2 nanostructure was used as a photoanode and Pt sputtered FTO glass was used as a counter cathode electrode. Ru based N719 dye was used as light sensitizer. For device, FTO (1.5 cm × 1.5 cm; 15 Ω, Asahi Glass Co. Ltd., Japan) substrates were first cleaned in a detergent solution using an ultrasonic bath for 20 min and then rinsed with water and ethanol successively and dried at 80 °C in an oven. Typically, 0.25 g of prepared TiO_2 samples was ultrasonically dispersed in 0.3 ml of acetic acid (99%) for 20 min. Further, 0.1 g of polyethylene glycol (MW 100 000) was added as binder and allowed to agitate for 2 h. As prepared TiO_2 paste was coated onto the cleaned FTO substrates using doctor blade technique to an average thickness of 20 μm and further the film was annealed at 500 °C for 1 h. The as-prepared TiO_2 photoanodic film with an area of 0.28 cm^2 was soaked in N719 dye for 24 h at ambient temperature. The dye-anchored electrode was then washed in ethanol to remove unbound dye and dried under vacuum for 15 min, and was sealed using a 30 μm thick spacer. All the TiO_2 photoelectrodes coated FTOs were treated with $TiCl_4$ solution and sintered. It was then sandwiched with the counter electrode of pt-sputtered FTO glass to form the cell. Electrolyte containing 0.1 M lithium iodide, 0.03 M iodine, 0.5 M 4-*tert*-butylpyridine, and 0.6 M 1-propyl-2,3-dimethyl imidazolium iodide in acetonitrile solvent was filled in the device.

(c) Characterization

A PANalytical (XPERT-PRO) X-ray diffractometer using Cu$K\alpha_1$ radiation ($\lambda = 1.5406$ Å) was employed to characterize

the crystallographic properties of the post-annealed samples. The surface morphologies of the samples were characterized by a field emission scanning electron microscope (FESEM, JEOL JSM). A transmission electron microscope (JEM-2010, JEOL USA Inc.) was employed to investigate the details of TiO_2 nanostructures. The surface area of prepared samples was dried under inert nitrogen (N_2) atmosphere for 12 h at 150 °C prior to BET measurements (under standard protocols at 77 K), and characterized using BET (NOVA 4200E Surface Area and Pore Size Analyzer, Quantachrome, USA). BET surface area has been averaged for three measurements and had an error average well within ± 3 m^2 g^{-1}. To prepare TEM samples, the post-annealed samples were placed onto a copper grid coated with carbon film. The samples were transferred and mounted inside a TEM Cu-ring. The thermal decomposition of TiO_2/PVAc composite nanofibers was measured by a thermo-gravimetric analyzer (TA Instruments TGA 2050) up to 800 °C with a heating rate of 5 °C min^{-1} under ambient atmosphere. Photocurrent measurements were carried out using a solar simulator (XES-151 S, San Ei, Japan) under AM1.5 G condition.

3. Result and discussion

3.1 Structural analysis

Fig. 1(a) shows the XRD pattern of the post-annealed TiO_2 hierarchical samples synthesized at temperature from 400 to

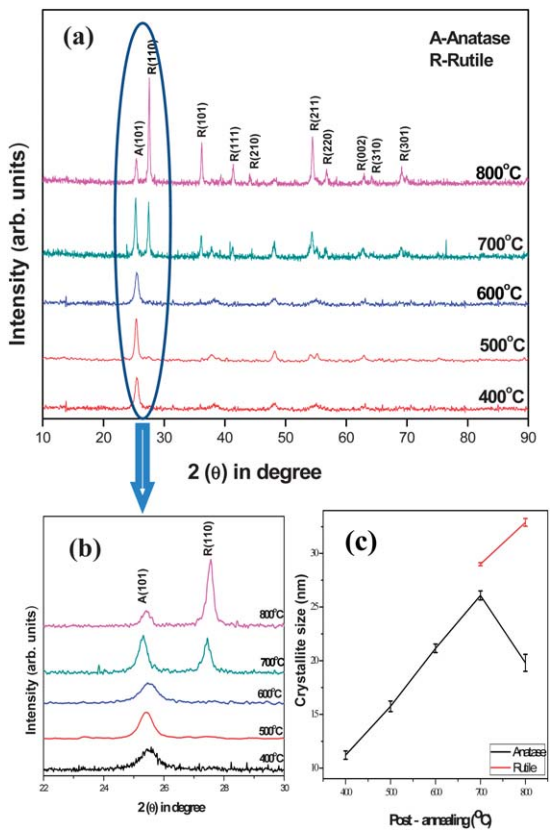

Fig. 1 XRD patterns of (a) hierarchical TiO_2 nanostructure samples prepared on different post-annealing electrospun fibres (b) selective area pattern of anatase (101) to rutile (110) phase formation and (c) crystallite size as a function of different growth temperatures.

800 °C. The samples annealed up to 600 °C exhibited a strong diffraction peak at 25.12° and other low intense diffraction peaks at $2(\theta) = 37.79°$, 48.26° and 54.12° with lattice constants of $a = 3.7852$ Å and $c = 9.493$ Å, indicating the formation of anatase phase TiO_2, which is shown in Fig. 1(b) (JCPDS#21-1272). The increase in peak intensities with the increase in annealing temperature revealed the enhancements in the crystallinity. No additional residual impurities were detected suggesting that the pure crystalline TiO_2 phase was formed. Upon increasing the annealing temperature to 700 °C, there was a formation of biphasic system (anatase–rutile) with strong diffraction peak at 25.36° and 27.54° corresponding to anatase (101) and rutile (110) plane respectively. Initial phase transformation at this condition is entirely due to decrease in crystallite size of anatase TiO_2 which results in the increase in the total boundary energy of TiO_2 samples. Further increase in annealing temperature to 800 °C shows the increase in rutile TiO_2 phase formation. The characteristic XRD pattern of the rutile structure which has space group of $P4_2/mnm$ with strong diffraction peaks at $2\theta = 27.4°$, 36.1°, 39.2°, 41.2°, 44.0°, 54.4°, and 56.7° can be indexed to the (110), (101), (200), (111), (210), (211), and (220) crystal planes of rutile TiO_2 (JCPDS card: 75-1755). However, a less intense peak at $2\theta = 25.3°$ remains for (101) plane of anatase TiO_2. As nucleation and growth mechanism are responsible for the transformation of anatase to rutile, an increased amount of nucleation sites favours rutile formation at higher temperatures. The calculated lattice constants are $a = 4.61$ Å and $c = 2.97$ Å, which coincide closely with the values of rutile TiO_2 from the JCPDS database (PDF#00-01-1292, $a = 4.58$ Å, $c = 2.95$ Å). Phase transformation also governed by structural defect and grain boundary concentration which can be expected to be increased with greater surface area. The post-annealing treatment enhances the crystallization of anatase, inhibits undesirable grain growth and retards the transformation of anatase to rutile phase. The rutile and anatase contents in the sample were estimated using the Spurr equation:[24]

$$F_R = \frac{1}{1 + 0.8[I_A(101)/I_R(110)]} \times 100 \quad (1)$$

$$F_A = 100 - \frac{1}{1 + 0.8[I_A(101)/I_R(110)]} \times 100 \quad (2)$$

where F_R and F_A are respectively, the mass fraction of rutile and anatase in the sample and I_A and I_R are the integrated intensities of the main peaks of anatase (101) and rutile (110), respectively. Detailed structural and phase content of different post-annealed samples are shown in Table 1. The average crystallite sizes of these post-annealed samples were calculated from the peak widths using the Scherrer equation[25] and detailed crystallite size as a function of different growth temperatures is shown in Fig. 1(c).

$$D = \frac{0.94\lambda}{\beta \cos\theta} \quad (3)$$

where D is the crystallite size, λ is the wavelength (1.546 Å for Cu Kα), β is the full-width at half-maximum (FWHM) of main intensity peak after subtraction of the equipment broadening and θ is the diffraction angle.

Table 1 Crystallite size, phase composition and surface analysis of hierarchical TiO_2 nanostructures electrodes at different annealing temperatures

		Anatase (101)		Rutile (110)		
Reaction temperature/°C	TiO_2 morphology	Phase content (%)	Crystallite size/nm	Phase content (%)	Crystallite size/nm	Surface area/m^2 g^{-1}
400	Spindle	100	12	—	–	23.68
500	Porous rod	100	16	—	—	75.74
600	Solid rod	100	22	—	—	69.78
700	Hollow tube	45.74	27	54.26	29	25.72
800	Spindle network	31.96	21	68.04	33	21.41

3.2 Surface analysis

Fig. 2(a)–(f) show the surface morphology of as-prepared TiO_2/PVAc fibers and annealed TiO_2 hierarchical nanostructures samples. The as-prepared samples show the formation of TiO_2/PVAc nanofibers with average diameters about 100–250 nm (Fig. 2(a)) and corresponding optical image of electrospun fibers deposited on Al collector (5 cm × 5 cm) is shown in the inset of Fig. 2(a). The electrospun composite fibers annealed at 400 °C show the formation of clustered spindle structure and corresponding TEM image (inset Fig. 2(b)) revealed that spindle structures with edge diameter ranging from ~100 nm and inner diameter up to ~200 nm were formed. Upon increasing the annealing temperature from 400 °C to 500 °C at 1 mbar, the spindle structure formulated to porous rods structure with an average length of 1.5 μm and a diameter of 150 nm as shown in Fig. 2(c). An increase in annealing to 600 °C showed the formation of recrystalline solid rod-like structure with a rod diameter of 200 nm and length greater than 1 μm as shown in Fig. 2(d).

Further increase in annealing temperature to 700 °C brought out biphasic hollow tubes diameter with 200 nm surrounded by fine aggregated nanoparticles, with formation of anatase (45.75%) and rutile (54.26%) mixed phase, which is confirmed by XRD observation shown in Fig. 1(a), and the corresponding TEM image is shown in Fig. 2(e) inset. Most recently, Mun *et al.*[26] have prepared TiO_2 based nanotubes by using metal anodic oxidation process, and found that the nanotube morphology enhanced performance of optical interferometric biosensor. Such TiO_2 nanotubes structure obtained just by the direct heat treatment process, without any template or surfactants has rarely been reported. When the annealing temperature reached to 800 °C, pure rutile : anatase (68.04 : 31.96) TiO_2 phase shaped in spindle like structure of diameter 200 nm is observed with the presence of small aggregated anatase TiO_2 particles in 50 nm in size (Fig. 2(f)).

Fig. 3(a)–(d) show the magnified FESEM and HRTEM images of porous TiO_2 nanorods sample annealed at 500 °C. The surface morphology shows that the porous nanorods structure with average pore size in-between individual grain boundary ranges from 5 to 10 nm, and the crystallite pore spacing is purely due to the deformation of insight polymer (PVAc). On closer examination, it can be seen that there are regions of individual

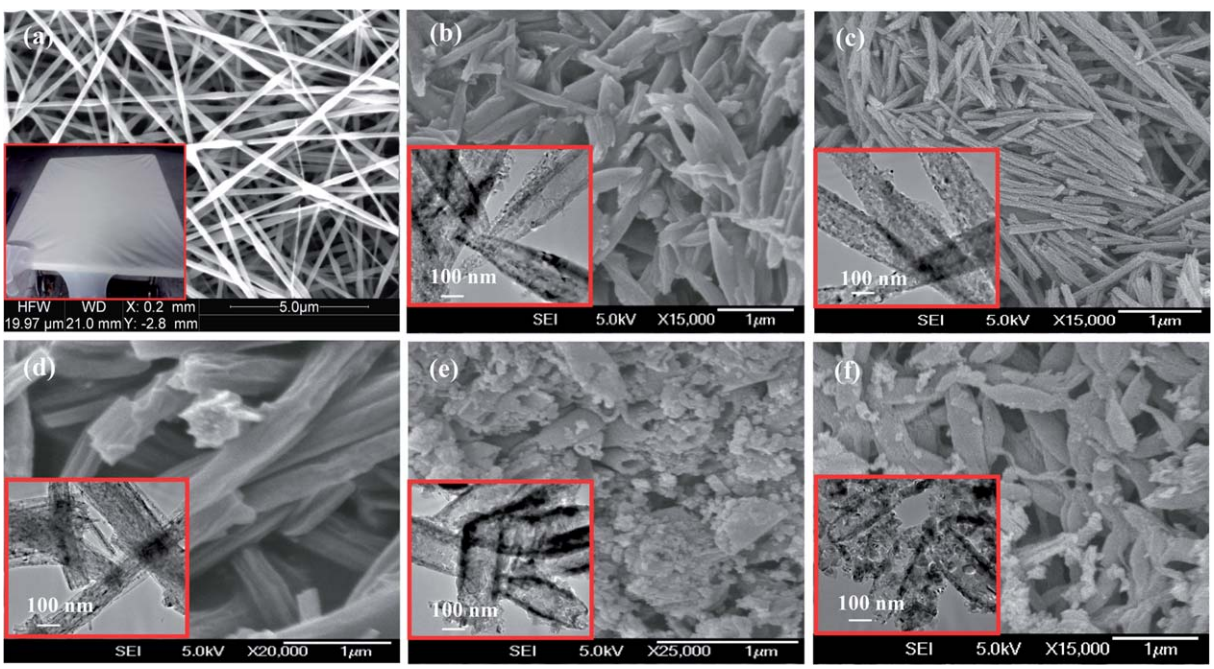

Fig. 2 FESEM images of hierarchical nanostructured TiO_2 samples (a) as-prepared TiO_2/PVAc electrospun fibres [optical photograph image inset], (b) 400 °C, (c) 500 °C, (d) 600 °C, (e) 700 °C and (f) 800 °C post-annealed electrospun fibers and corresponding inset figures show the TEM images.

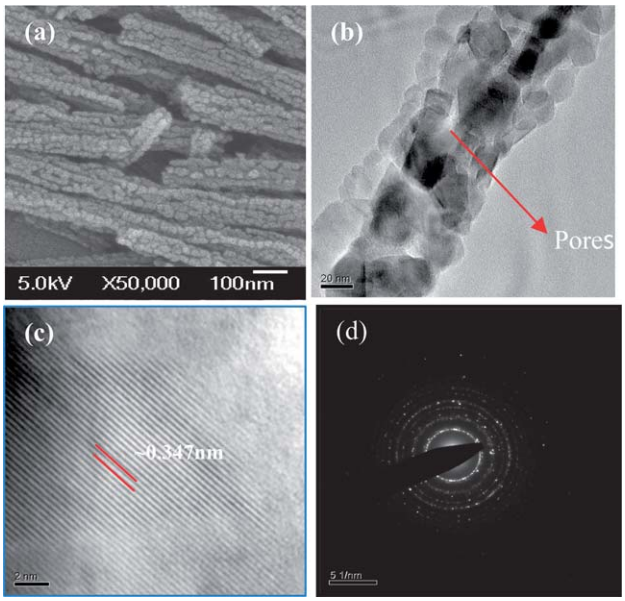

Fig. 3 (a–c) FESEM and corresponding TEM/HRTEM images and (d) SAED diffraction pattern of porous TiO_2 nanorods prepared at 500 °C.

spherical particles with wall diameter around 10–15 nm as shown in Fig. 3(b). HRTEM image confirms that the prepared porous TiO_2 rod has high crystalline nature with the lattice spacing of 0.347 nm, corresponding to (101) planes of TiO_2 porous-rod structure with a diameter of 50 nm. The corresponding selected area electron diffraction (SAED) pattern shown in Fig. 3(d) confirms highly crystalline nature of anatase TiO_2.

The HRTEM image of the sample annealed at 700 °C clearly confirmed the highly ordered crystalline nature of rutile hollow tube and surrounded anatase particles with the lattice spacings of 0.321 nm and 0.349 nm were formed upon annealing at 700 °C, as shown in Fig. 4(b). It is noteworthy that selected area electron diffraction (SAED) data showed diffraction rings, not single reflections, indicating that the crystallites were more or less randomly oriented within the tube walls. The pure mixed phase of TiO_2 was evidenced from SAED and HRTEM analysis. With an aim to develop and better understand the morphological evolution of TiO_2 nanostructures, high resolution and helium (He) ion spectroscopy analyses were carried out. The high resolution He-ion image confirmed the formation of hollow tubes structure with an inner core diameter of around ~70 nm and an outer wall thickness of 30 nm, shown in Fig. 4(c)–(e). The specific surface area is strongly related to the exterior particle size confinement. It is known that the surface area generally increases with decreasing grain boundaries. The BET surface area of the porous TiO_2 rod structures revealed the higher surface area of 75 $m^2 g^{-1}$ was achieved for TiO_2 porous rod structure obtained at 500 °C due to its lower grain size, whereas for tubes and rods obtained at 600 °C and 700 °C yielded a lower surface area of ~20 to 25 $m^2 g^{-1}$, which could be due to the larger diameter size of about 100 nm. The detailed surface analysis data are provided in Table 1.

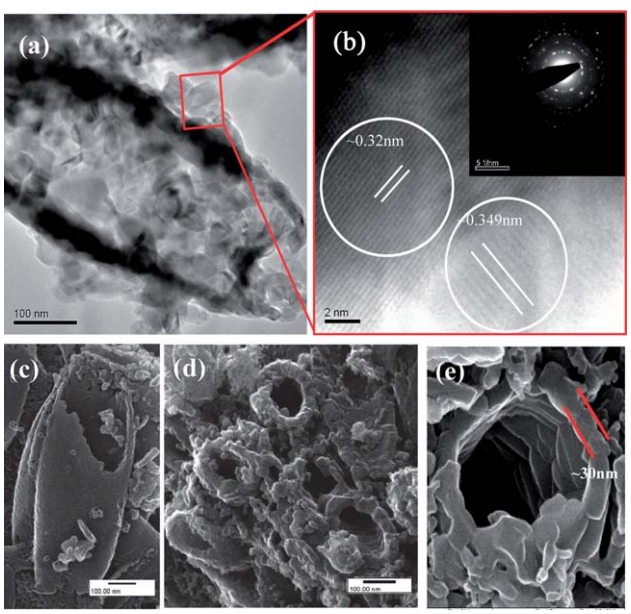

Fig. 4 (a and b) TEM/HRTEM images and inset image show the SAED diffraction pattern and correspondingly (c)–(e) show the low and high magnified Helium (He) ion spectroscopy images of biphasic hollow TiO_2 nanotubes prepared by annealing at 700 °C.

3.3 TGA analysis

From our TGA analysis, thermogravimetric analysis (TGA) measures the amount and rate of change in the weight of a material as a function of temperature in a controlled atmosphere. As shown in Fig. 5, the 10% weight loss before 150 °C resulted from the evaporation of moisture and solvent in the TiO_2/PVAc composite nanofibers. Later, a steep decrease in weight loss of about 63.1% around 250 to 400 °C was observed which corresponds to the initial decomposition of PVAc polymer in TiO_2 composite fibers. The exact polymer decomposition temperature in the composite was found to be around 336 °C, which was evident from Fig. 5. As the annealing temperature was raised to 500 °C, an additional 14.9% weight loss was observed in the TGA profile. Subsequent loss in weight was attributed to the removal of residual polymer aggregates. Further increase in the

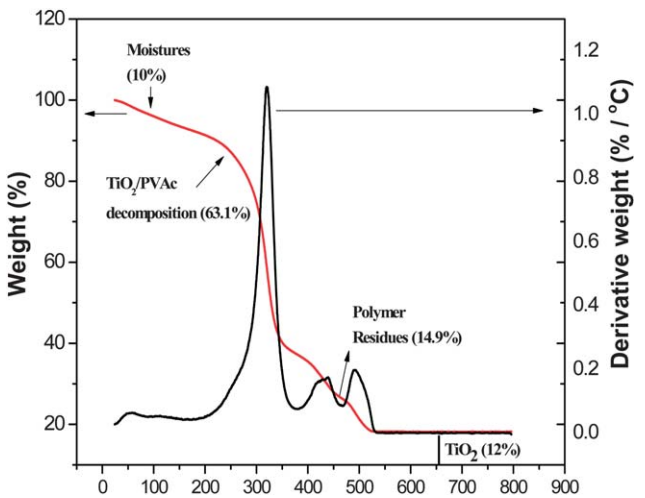

Fig. 5 TGA analysis of TiO_2/PVAc composite fibers.

annealing temperature to 800 °C, a smooth tail with no weight loss was observed. Finally, white powder with net 12 wt% of pure TiO_2 phase characteristics was obtained as end product, which was confirmed by XRD pattern (Fig. 1).

4. Formation and growth mechanism

To investigate the growth mechanism of the pure anatase, rutile–anatase hierarchical TiO_2 nanostructures, a series of systematic experiments were carried out at various temperatures. The growth formation of different hierarchical TiO_2 nanostructures was occurred in two regions: (a) polymer PVAc deformation region and (b) crystallite reformation region as shown in Fig. 6. Firstly, pure TiO_2 phase formation was not occurred at 400 °C, due to its initial decomposition of organic polymer (PVAc) residues and outgassing of polymer (Fig. 5). At this temperature, the weight loss was drastic *i.e.* about 63.1%, which caused shrinkage and swelling in the fibers, leading to the formation of spindle-like morphology. Further increasing of temperature to 500 °C, still a significant 15% weight loss was observed that was associated with the removal of all the remaining polymer residues. This created the formation of porous sites which caused the separation of individual spherical particles of diameter 10–15 nm present in the nanorod, also confirmed by HRTEM and FESEM images (Fig. 3(a) and (b)). These crystallite particles at 500 °C increase the surface to volume ratio of the rod morphology which is evident from the BET measured surface area of 75 $m^2\ g^{-1}$ in porous TiO_2 nanorods than other hierarchical TiO_2 nanostructures. In the region between 600 and 800 °C, the increase in post-annealing temperature progressively showed the growth of different hierarchical TiO_2 structures with the changes in crystallite phase reformation. The porous TiO_2 nanorods structure was transformed into solid rod like structure when annealing temperature was increased from 500 °C to 600 °C. The average grain size

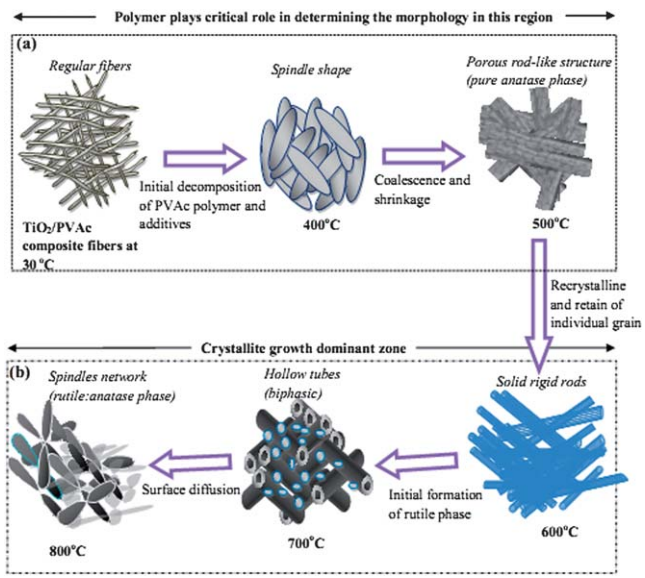

Fig. 6 Formation process of different hierarchical TiO_2 nanostructures: (a) polymer deformation region and (b) crystallite reformation region.

determined by XRD patterns and Scherrer calculation showed that pure anatase (100%) TiO_2 was retained at 600 °C, but the crystallite size increased from 16 nm to 22 nm. This increase in crystallite growth boundaries eventually deformed the existing porous sites which transformed into solid rod like structures as observed in FESEM image (Fig. 2(c) and (d). At 700 °C, a drastic change was seen in both crystal phase and TiO_2 rods morphology. The pure anatase of TiO_2 nanorods was transformed at 700 °C into TiO_2 hollow tubes with stoichiometry phase compositions of 45.74% anatase and 54.25% rutile. This can be explained as follows; the anatase TiO_2 nanorods undergo orientation and deform into nanoparticles at this temperature, while the rutile grains continue to grow. Material densification was occurred due to the anatase-to-rutile transformation that drives out the anatase TiO_2 nanoparticles present in the core part of the rods, which led to the formation of hollow tube structure. The anatase TiO_2 nanoparticles were observed on the walls of the rutile hollow tubes, which are confirmed by HRTEM analysis (Fig. 4(b)). The available TiO_2 nanoparticles that start to grow by consuming neighbours *via* surface diffusion from tube walls could be likened to Ostwald ripening.[27] Further increase in temperature to 800 °C, more conversion of anatase phase into rutile was occurred. The spindle shaped morphology was observed with the phase composition of 32% anatase and 68% rutile. As the mass density of rutile (110) phase is higher than that of anatase (101) and the stoichiometry ratio of rutile to anatase is 2 : 1, the tubes especially edges suffer from the rutile mass exertion that transforms them into spindle like structure. From the entire post-annealing process *i.e.* from 400 to 800 °C done with a controlled ramp rate of 5 °C min^{-1} and PVAc as the spinnable polymer additive to TiO_2 precursor (MW: 5×10^5), it is interesting to observe that the TiO_2 nanofibers transformed to different structures: nanorods, tubes, and spindles, and phases; pure anatase, biphasic, and pure rutile through the simple single step growth process without the chemical surface treatment and template method. Further studies are necessary to understand the behaviour of these hierarchical structures in device applications.

5. Device performance

Fig. 7 shows the photocurrent density *vs.* voltage (*J*–*V*) curves of DSSCs fabricated with the hierarchical nanostructured TiO_2 materials as photoanode film of thickness 20 μm under simulated air mass 1.5 global (AM1.5 G). The resultant photovoltaic parameters: open-circuit voltage (V_{oc}), short-circuit current density (J_{sc}), fill factor (FF) and the conversion efficiency (η) are summarized in Table 2. From Table 2, it is very clear that the structural morphology played a significant role in the solar cell performance. The porous TiO_2 nanorods morphology shows the largest current density (I_{sc}) of 8.61 mA cm^{-2} among other morphologies, which in turn enhanced the conversion efficiency of 4.56%. This is due to higher surface area that facilitated for loading of larger number of dye molecules on the surface of TiO_2 porous rods. The pure anatase TiO_2 with a surface area of 69 $m^2\ g^{-1}$ obtained at 600 °C was expected to deliver higher efficiency, but resulted in a lower efficiency of 2.5% which attributed to the poor dye loading onto the very smooth solid nanorods surface.

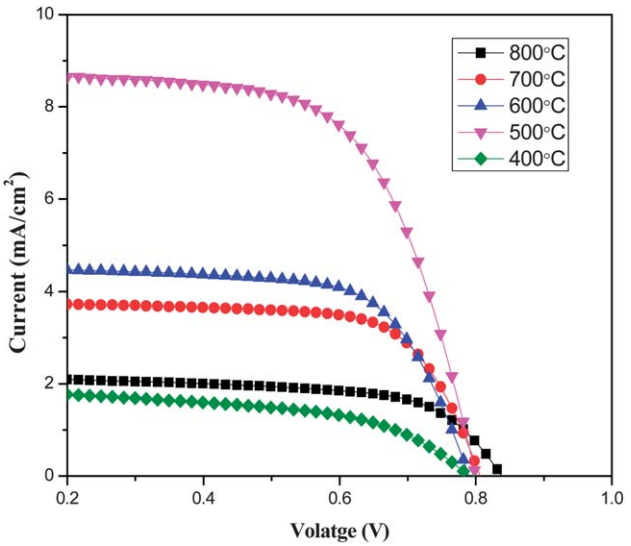

Fig. 7 Photocurrent density–voltage characteristics of DSSCs with different hierarchical TiO_2 nanostructure electrodes.

Table 2 Device characteristics of DSSCs with different hierarchical TiO_2 nanostructure electrodes

Annealing temperature/°C	Hierarchical TiO_2 morphology	V_{oc}/ V	J_{sc}/mA cm^{-2}	FF (%)	η (%)
400	Spindle	0.765	1.98	52.1	0.79
500	Porous rod	0.798	8.61	66.3	4.56
600	Rod structure	0.782	4.55	69.5	2.47
700	Hollow tube	0.798	3.79	71.5	2.16
800	Spindle network	0.832	2.18	64.6	1.17

6. Conclusions

In summary, a pure anatase, mixed, and pure rutile TiO_2 phases based hierarchical nanorods, nanotubes, and nanospindles structures were synthesized from electrospun composite fibers by controlled annealing at temperatures from 400 to 800 °C, at 1 mbar, and with a ramp rate of 5 °C min^{-1}. This method eliminated the need for surfactants and templates. By varying the growth conditions, the crystallographic structural orientation from pure anatase (101) to pure rutile (110) phase was demonstrated. The transformation of regular fibers to porous rod/hollow tube structure, and to spindle network structure with diameter around 100–150 nm was influenced by polymer degradation and crystallite reformation processes. Highly porous TiO_2 nanorods obtained at 500 °C showed an overall conversion efficiency (η) of 4.56% in DSSC with the I_{sc} of 8.61 mA cm^{-2} and the V_{oc} of 0.582 V. Further efforts aiming to confined rods/tubes diameter and reduce the TiO_2 electrode film thickness to enhance the efficiency DSSC are under study. This present growth strategy has considerable potentiality to provide a morphologically controllable route, hence this study can further be extended to other semiconducting metal oxide nanostructures, thus for a wide variety of applications include photo-catalysts for environmental remediation, sensors electrode and photonic materials.

Acknowledgements

This work was supported by Singapore NRF-CRP grant on "Nanonets for Harnessing Solar Energy and Storage" and also NUS and NTU for providing facilities to carry out the research. Dr V. Thavasi acknowledges NUSNNI for support.

References

1 X. Chen and S. S. Mao, *Chem. Rev.*, 2007, **107**, 2891.
2 A. S. Barnard and L. A. Curtiss, *Nano Lett.*, 2005, **5**, 1261.
3 S. K. Choi, S. Kim, S. K. Lim and H. Park, *J. Phys. Chem. C*, 2010, **114**, 16475.
4 F. Sauvage, D. Chen, P. Comte, F. Huang, L. P. Heiniger, Y. B. Cheng, R. A. Caruso and M. Graetzel, *ACS Nano*, 2010, **4**, 4420.
5 S. H. Nam, H. S. Shim, Y. S. Kim, M. A. Dar, J. G. Kim and W. B. Kim, *ACS Appl. Mater. Interfaces*, 2010, **2**, 2046.
6 Y. Zhang, P. Xiao, X. Zhou, D. Liu, B. B. Garciaa and G. Cao, *J. Mater. Chem.*, 2009, **19**, 948.
7 N. M. Bedford and A. J. Steckl, *ACS Appl. Mater. Interfaces*, 2010, **2**, 2448.
8 G. Fu, P. S. Vary and C. T. Lin, *J. Phys. Chem. B*, 2005, **109**, 8889.
9 C. Wang, C. Shao, Y. Liu and X. Li, *Inorg. Chem.*, 2009, **48**, 1105.
10 L. Chen, M. E. Graham, G. Li and K. A. Gray, *Thin Solid Films*, 2006, **515**, 1176.
11 S. W. Kim, T. H. Han, J. Kim, H. Gwon, H. S. Moon, S. W. Kang, S. O. Kim and K. Kang, *ACS Nano*, 2009, **3**, 1085.
12 F. Shao, J. Sun, L. Gao, S. Yang and J. Luo, *J. Phys. Chem. C*, 2011, **115**, 1819.
13 F. Sauvage, F. Di Fonzo, A. Li Bassi, C. S. Casari, V. Russo, G. Divitini, C. Ducati, C. E. Bottani, P. Comte and M. Graetzel, *Nano Lett.*, 2010, **10**, 2562.
14 E. Ghadiri, N. Taghavinia, S. M. Zakeeruddin, M. Gratzel and J. E. Moser, *Nano Lett.*, 2010, **10**, 1632.
15 J. M. Wu, H. Shih and W. T. Wu, *Nanotechnology*, 2006, **17**, 105.
16 S. J. Song, Y. J. Park, J. Park, M. D. Cho, J. H. Kim, M. H. Jeong, Y. S. Kim and D. L. Cho, *J. Mater. Chem.*, 2010, **20**, 4792.
17 L. K. Tan, M. A. S. Chong and H. Gao, *J. Phys. Chem. C*, 2008, **112**, 69.
18 J. Yu, Q. Xiang, J. Ran and S. Mann, *CrystEngComm*, 2010, **12**, 872.
19 X. Zhang, X. Ge and C. Wang, *Cryst. Growth Des.*, 2009, **9**, 4301.
20 M. K. Aminian, N. Taghavinia, A. Iraji-zad, S. M. Mahdavi, M. Chavoshi and S. Ahmadian, *Nanotechnology*, 2006, **17**, 520.
21 L. Li and C. Liu, *CrystEngComm*, 2010, **12**, 2073.
22 L. Yang, Q. Cai and Y. Yu, *Inorg. Chem.*, 2006, **45**, 9616.
23 X. Chen and S. S. Mao, *Chem. Rev.*, 2007, **107**, 2891.
24 R. A. Spurr and W. Myers, *Anal. Chem.*, 1957, **29**, 760.
25 B. D. Cullity, *Elements of X-Ray Diffractions*, Addison-Wesley, MA, 1978, 102.
26 K. S. Mun, S. D. Alvarez, W. Y. Choi and M. J. Sailor, *ACS Nano*, 2010, **4**, 2070.
27 C. J. Barbe, F. Arendse, P. Comte, M. Jirousek, F. Lenzmann, V. Shklover and M. Gratzel, *J. Am. Ceram. Soc.*, 1997, **80**, 3157.